Microstructure evolution for isothermal sintering of binder jet 3D printed alloy 625 above and below the solidus temperature

Chuyuan Zheng [a,1], Amir Mostafaei [a,b,1], Pierangeli Rodriguez de Vecchis [a], Ian Nettleship [a] , Markus Chmielus [a,*]

[a] Department of Mechanical Engineering and Materials Science, University of Pittsburgh, Pittsburgh, PA 15261, USA

[b] Department of Mechanical, Materials, and Aerospace Engineering, Illinois Institute of Technology, 10 W 32nd Street, Chicago, IL 60616, USA

[1] These two authors contributed equally to this work.

* Corresponding author: M. Chmielus, chmielus@pitt.edu

Email addresses: chz47@pitt.edu (C. Zheng), mostafaei@iit.edu (A. Mostafaei), pir6@pitt.edu (P. Rodriguez de Vecchis), nettles@pitt.edu (I. Nettleship), chmielus@pitt.edu (M. Chmielus)

Abstract

When compared to beam-based melting methods, binder jet 3D printing is less time consuming, and the printed material is less prone to residual stresses. However, binder jet printing often contains remnant porosity that survives pressureless sintering and limits the mechanical properties of metals including fatigue strength and ductility. In this work, gas atomized nickel-based superalloy 625 powders with three different particle size distributions are binder jet printed and subsequently isothermally sintered at subsolidus and supersolidus temperatures. Individual feature measurements were conducted on two-dimensional sections and pore size distribution frequencies were plotted to reveal the difference in microstructural evolution between subsolidus and supersolidus sintering. Supersolidus liquid phase sintering is thought to have facilitated particle rearrangement under the surface tension of the liquid phase, resulting in a homogeneous microstructure that favored subsequent densification and higher final density. Additionally, printed powder with a wide particle size distribution not only reached high green density of ~52%, but also achieved final densities above 99%.

Keywords: Additive Manufacturing; Inconel 625; Densification kinetics; subsolidus solid-state sintering; Supersolidus liquid phase sintering; Microstructure analysis.

1. Introduction

In recent decades, substantial progress has been made in the understanding, development and utilization of additive manufacturing processes. Binder jet 3D printing (BJ3DP), a non-beam based additive manufacturing (AM) method, refers to the technology in which powdered material is deposited layer-by-layer and selectively joined in each layer with a thermosetting binder[1]. The deposited material requires sintering and if high density is required, post-sintering processes such as hot isostatic pressing (HIP-ping) are often necessary to ensure the consolidation and removal of defects

generated during the printing process. BJ3DP holds distinct advantages when compared to other additive manufacturing technologies applied to metal powders. These include significantly expedited rate of production, increased freedom of designing for complex shapes, and the ability to produce residual stress-free printed structures [2].

BJ3DP has been successfully applied to metals such as nickel-based superalloys [3–5], titanium [6–8], steels [9–14], Co-Cr [15,16], magnetic shape memory alloys [17–20], and copper [21–24]. However, there are only a few studies focused on the microstructural evolution of sintered BJ3DP materials, especially nickel-based superalloys. A study on BJ3DP alloy 718 by Nandwana et al. [3] suggested that particle size distribution (PSD) is one of the key factors determining the final density of binder jetted material after sintering, by the means of affecting the particle packing arrangement, hence green density, as well as sintering kinetics. They also pointed out that supersolidus liquid phase sintering (SLPS) is necessary to achieve full density for alloy 718. The majority of the large pores introduced during the binder jetting process are attributed to the liquid-solid interactions between the binder and powder particles resulting in interlayer voids and printing lines caused by ballistic ejection [25]. Parab et al. [26] showed when fine powder particles were binder jetted, the transferred momentum from the binder to powder particles can cause changes in the powder bed. The resulting powder-binder interaction leads to the formation of sub-surface pores in printed parts; therefore, a continuous gap between printed layers might be seen. In contrast, when coarse particles were binder jetted, powder ejection from the powder bed surface was problematic. If the number of ejected powders is large and the formed gap is not refilled by the subsequent layer, large pores will appear in the final 3D printed part. It is thought that broadening the PSD allows small particles to fill in the printing defects between the printing layers and lines, resulting in a more homogeneous green microstructure that will favor pore elimination in sintering.

A previous study by Mostafaei et al. [27] on the effect of PSD on the densification behavior of alloy 625 indicated that using wide PSD powder as the feedstock for BJ3DP, resulted in higher green and final densities for the binder jetted materials. On the other hand, this study also showed that subsolidus solid-state sintering of the printed materials, regardless of PSD, lead to low final density even at prolonged sintering times. The role of microstructural evolution in these very different outcomes of isothermal sintering was not addressed. Therefore, the aim of this work is to show how PSD affected microstructural evolution of a binder jetted alloy 625 during supersolidus sintering and subsolidus sintering.

2. Experimental Procedures

Air-melted nitrogen atomized alloy 625 powders were obtained from Carpenter Technology Corporation as the powder feedstock for binder jet 3D printing. 10 kg of powder was sieved through a series of meshes, and three particle size ranges were prepared, namely 53-63 μm (C, for coarse), 16-25 μm (F, for fine), and the original range 16-63 μm (W, for wide). The morphology of the three atomized alloy 625 powders was observed using a ZEISS Sigma 500 VP scanning electron microscope (SEM) and representative micrographs are shown in Figure 1 (top). The volume percentile PSD was

analyzed using a Microtrac S3500 tri-laser diffraction particle analysis system via algorithms for spherical particles. The fluid used in the analysis was prepared using ~1 g of powder suspended in isopropyl alcohol. The PSD results of all three powder are illustrated in Figure 1 (bottom).

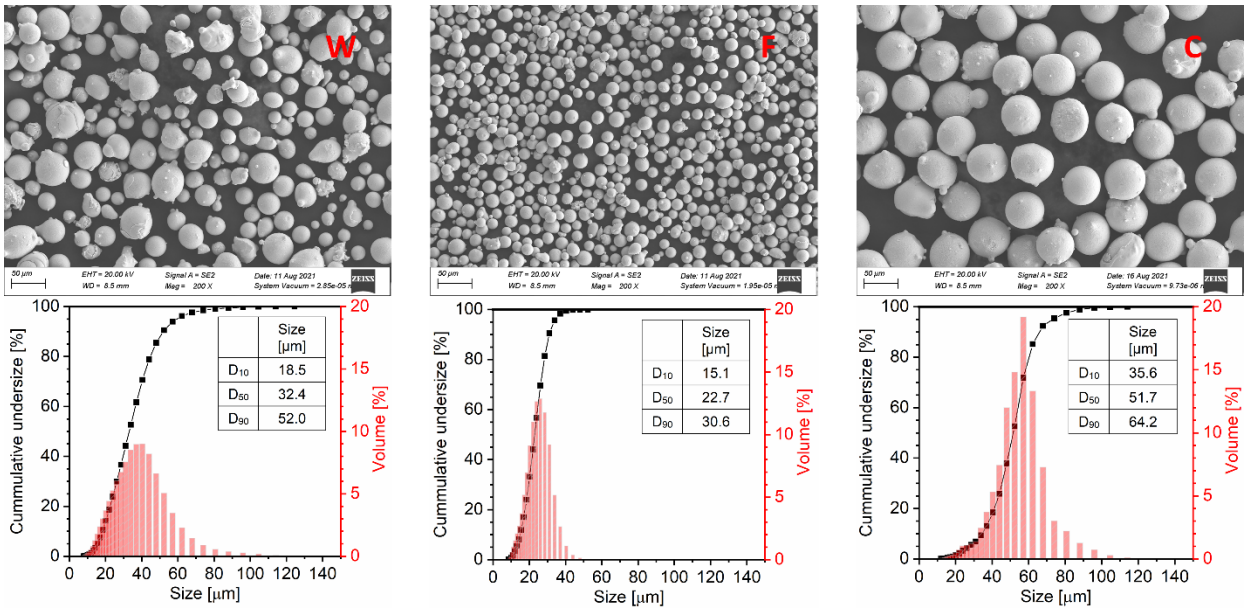

Figure 1. (top) SEM micrographs and (bottom) Cumulative volume percentile results for the three different powder size distributions of 625 alloy used in the study.

The binder jet printing process was carried out in an ExOne X-1 Lab 3D printer with the following processing parameters: 100 μm layer thickness, binder saturation of 60%, spread speed of 15 mm/s, feed powder to layer thickness ratio of 2, heater power control (intensity of the heat lamp as it hovers over the powder bed) set to 70% and drying time of 40 s. Green bodies were printed in two shapes: a cuboidal shape of 12x10x10 mm^3, and a cylindrical shape with 7 mm in both height and diameter. For each printing batch, 12 samples were printed in a 3-by-4 matrix on the print bed. We observed negligible variation in green densities between the green bodies, regardless of the powder size used or the relative positions in the powder bed, due to the small build box volume of the X-1 Lab printer, although significant green density variations were reported using different binder jet printers [28]. After printing, the green bodies underwent a binder curing process at 200 °C for 8 h followed by a depowdering process to remove excess loose powders. Then relative green densities of 51.5 ± 1.1%, 45 ± 1.2% and 47.5 ± 0.7% were measured for the W, F and C powders, respectively. The cured samples were placed in a Lindberg tube furnace under vacuum for sintering at 1270 °C (subsolidus) and 1285 °C (supersolidus). According to the thermocouple calibration data, the heat zone has a variation of 1.4 °C when reached isothermal sintering temperature. Our previous study [4] indicated that the solidus temperature for as-received powder (prior to sieving) was 1283 °C. The heating profile was set as follows: 5 °C/min from room temperature to 600 °C,

then 3.2 °C/min to 1000 °C, and 2.8 °C/min to the designated sintering temperatures (1270 or 1285 °C). Once reached the designated sintering temperature, isothermal sintering was conducted with controlled time durations (0, 0.5, 1, 2, 4, 8 and 12 h) followed by controlled furnace cooling to room temperature. The full heating and cooling profiles may be found elsewhere [29]. Three technical repeats were sintered for each PSD and sintering condition. The samples were oriented as taken from the printer, that is, with the *x*-*y* top surface upwards and were placed approximately 5 mm apart in the furnace.

Characterization for the samples was carried out in both their green and sintered states. Bulk densities were measured using the water immersion method, also known as Archimedes method (the theoretical density of alloy 625 (i.e. 8.44 g/cm^3) and details were given in [27]. Sintered samples were sectioned using a diamond saw along the direction parallel to the build direction of the binder-jet printer (z-axis), so that the inter-layer defects and features were preserved and were visible under optical microscopy. The sectioned samples were then cold-mounted and polished using 9 μm and then 3μm DiaPro Dac diamond polishing agents, and finally OP-S colloidal silica for mechanical etching (all supplied by Struers Inc., USA). For the final polishing process, the OP-S silica is an alkaline suspension with minimal etching effect on nickel-based alloys, but with substantial polishing time revealed the grain structure. Therefore, stereological measurements such as grain intercepts could be measured on these polished surfaces. Micrographs of ground and polished sections were taken using a Zeiss SmartZoom 5 optical microscope with a resolution of 2.20 μm/pixel. These micrographs were processed and analyzed, either by traditional grain boundary and pore boundary counting techniques [30] or by using an open-source software ImageJ to obtain population data for thresholded pore sections. For OM feature measurements, five micrographs were taken on the sectioned surface of each sample. The pore section size information was summed for these images before generating distribution plots. For any sample, the total feature counted exceeded 300 to ensure statistical significance. The pore sections were thresholded prior to the auto-processing by ImageJ. Bulk density data were used as an independent check of the binary threshold level to make sure the pore boundaries were segmented accurately. Detailed information on how the grain intercept, pore intercept and pore separation are calculated can be found in [27].

3. Results

3.1. Subsolidus solid state sintering

Isothermal sintering at 1270 °C, below the solidus, resulted in solid state sintering and an increase in density from 70% to 85% over 12 h. Figure 2 shows the linear shrinkage data for samples after sintering and measured along different directions. The linear shrinkage for all samples were very similar in *x*- and *y*-direction, hence an average of *x*- and *y*-shrinkages is plotted here in comparison with in z-direction. It can be readily observed that for all samples the shrinkage along *z*-direction is larger than the shrinkage along *x*/y-direction. Specifically for powder F, the *z*-shrinkage exceeds *x*/y-shrinkage by more than 4% when the sintering time is longer than 1 h.

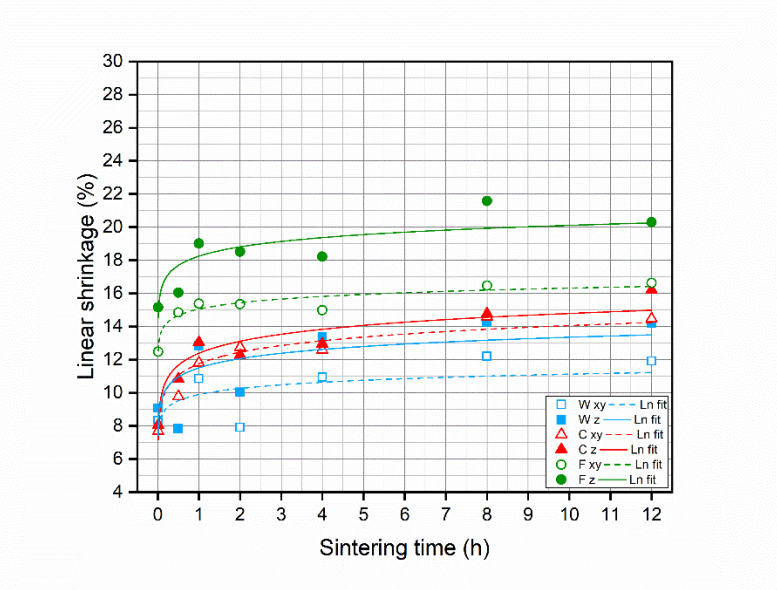

Figure 2. Linear shrinkage of samples sintered at 1270 °C for powder W (blue), F (green), and C (red), measured in *x/y*- and *z*-direction. Curves show lognormal fitting of the shrinkage.

Figure 3 shows a comparison of bulk density measured by the immersion method and the solid area fraction determined from the optical microscopy images. In general, there is good agreement and so the sections used for microscopy are considered representative of the material. At short times, less than 1 h, the wide particle size distribution (W) showed relatively rapid increase in relative bulk density to 82% and then for the remaining 11 h there was very little further increase in density as shown in Figure 3. Additionally, microstructural evolution was studied by measuring grain and pore size as functions of holding time. For powder W, there was an increase in grain intercept, pore intercept and pore separation throughout the 12 h of isothermal sintering at 1270 °C, as shown in Figure 4 (a-c) suggesting that the microstructure was coarsening.

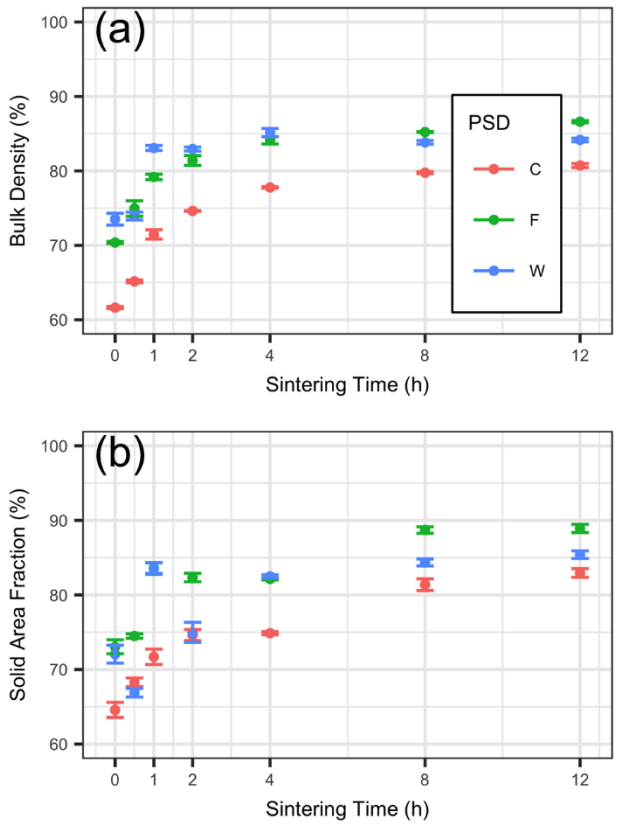

Figure 3. The effect of sintering time on (a) the relative bulk density measured using the Archimedes method and (b) solid area fraction measured on optical micrographs of polished sections for: powder W, powder F and powder C sintered at 1270 °C.

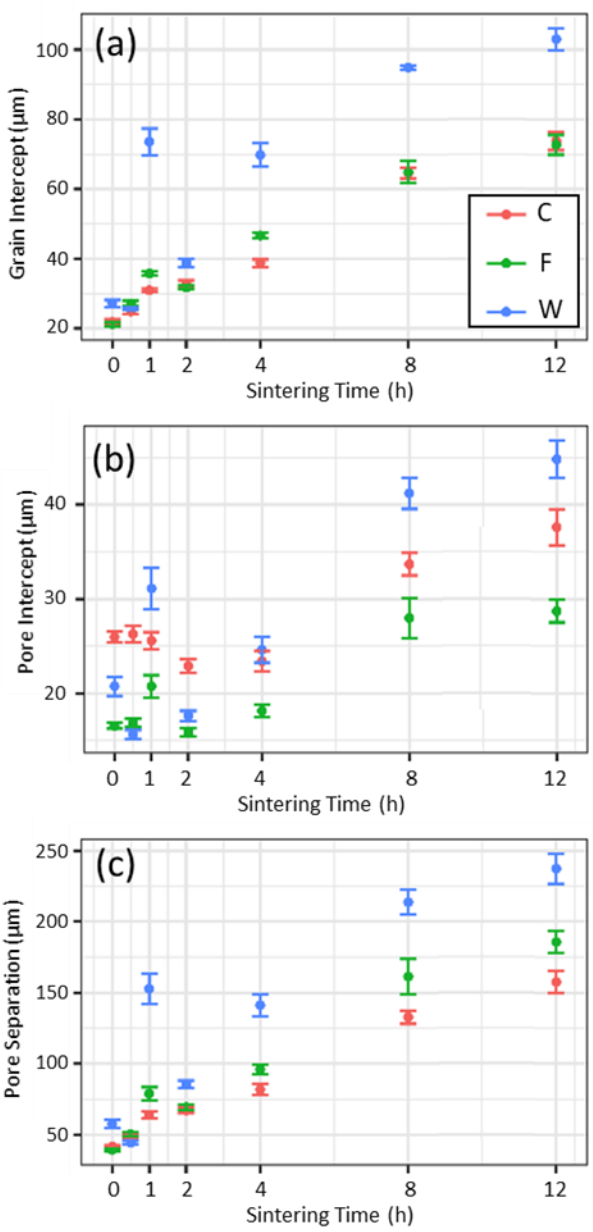

Figure 4. The effect of sintering time on (a) grain intercept, (b) pore intercept and (c) pore separation at 1270 °C for powder W, powder F and powder C.

Figure 5 (a) shows the evolution of the pore area distribution for powder W, counted as number frequency as a function of sintering time at 1270 °C. During the first hour while the density was increasing, the shape of pore size distribution was relatively broad, extending from 10 μm^2 to over 10,000 μm^2. Then at longer times there was preferential removal of the smaller pore sections under 100 μm^2 and the emergence of a sharper peak above 1,000 μm^2, probably due to neck growth between the particles. This allowed more grain growth and lead to the observed increase in the grain intercept and the pore separation. To take into account the increase in density, Figure 5 (d) shows the same information for pores counted by absolute number from the same section area

rather than pore fraction. This shows that the frequencies in all the size ranges decreased with increased sintering time although the decrease is less rapid in the larger pore section size intervals above 1,000 μm^2. In consequence, it is very unlikely that the observed increase in pore intercept in Figure 4 (b) was due to individual pores coarsening. In contrast, the associated increase in the diffusion length was actually caused by the elimination of the smaller pore sections. This is characteristic of sintering of microstructures that are spatially heterogeneous, due to the presence of particle aggregates or particle packing defects [31,32], the resulting pore section elimination contributed to the exhaustion of densification at this temperature. This is demonstrated in Figure 6 which shows the optical micrographs of the sintered samples. Figure 6 (a) shows the final microstructure of powder W after sintering at 1270 °C for 12 h. The remaining pore sections were heterogeneously dispersed in a microstructure that exhibits regions that were pore free and some relatively large irregular pore sections.

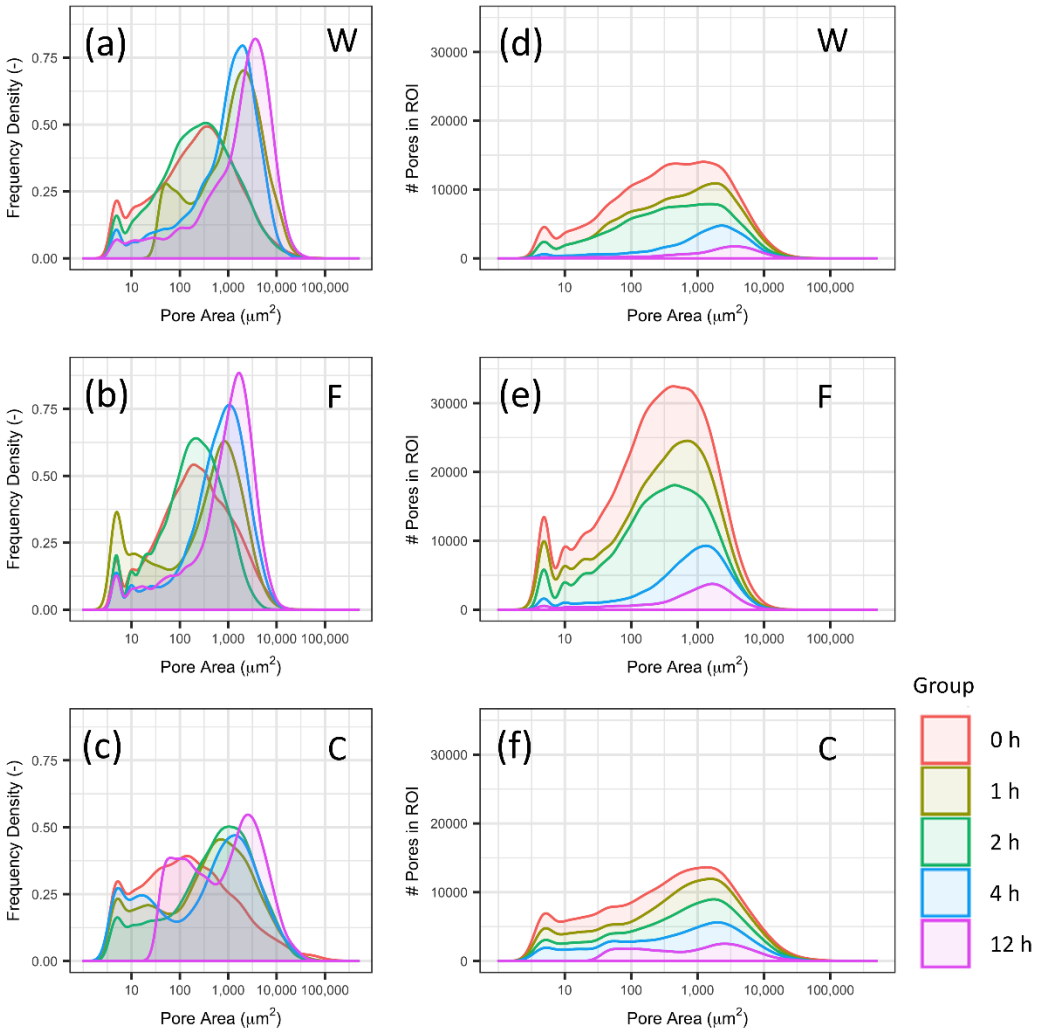

Figure 5. Pore size distributions for (a,d) powder W, (b,e) powder F, and (c,f) powder C sintered for different times ranging between 0-12 h at 1270 °C. (a-c) are based on the relative number frequency whereas (d-f) are based on the absolute number count in the region of interest.

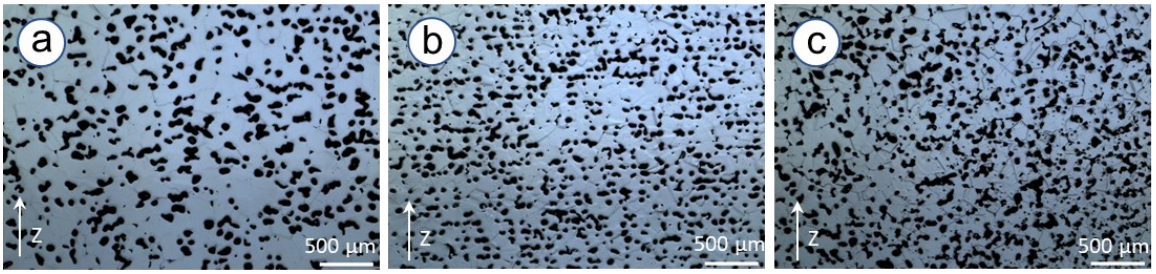

Figure 6. Micrographs of the 625 samples sintered for 12 h at 1270 °C. (a) powder W (16-63 µm), (b) powder F (16-25 µm) and (c) powder C (53-63 µm). The solid area fraction (SAF) values obtained from images are 85.4%, 88.9% and 83.0%, respectively.

Powder F showed an increase in density from 70% to ~82% within the first two hours at 1270 °C. Then, there was little further densification at longer sintering times. In this time frame, Figure 4 shows that, again, there was an increase in grain intercept, pore intercept and pore separation throughout isothermal sintering at 1270 °C. However, the extent of the increase was less than for powder W over the same time period even though the density was approximately the same. Figure 5 (b) shows, in general, the behavior of the pore size distribution for powder F was like powder W. The increase in the peak in pore section area above 1,000 μm^2 was obvious and when the increase in density is taken into account in (e), it is clear that the peak at large pore sections was due to the fact that larger pore sections were being removed more slowly than the finer pore sections.

Figure 6 (b) shows the microstructure of powder F after 12 h at 1270 °C. Small pore sections were more numerous than for powder W sintered under the same conditions, but the pore sections were clearly aligned parallel to print layers. It should be noted that the sectioning planes for optical microscopy is perpendicular to z-axis, or the build direction during printing. In the previous work [27], it was demonstrated that while fine particles can improve the packing efficiency, in a binder jet printed system they tend to agglomerate during layer spreading [26]. Consequently, when the layer thickness was held constant, the narrowed PSD reduces the transmission of compressive load to the interlayer regions during particle spreading and therefore produced, periodically concentrated, highly aligned interlayer defects. This is further explained in the Discussion section (section 4). These pores are expected to be the larger pore areas in the distribution and clearly survive sintering to a significant extent.

Powder C shows an increase in density during the first four hours of sintering at 1270 °C with a small increase in density at longer times. The grain intercept, pore intercept and pore separation increased continuously through the 12 h similarly to that seen for powder F. Again, Figure 5 (c) shows that this increase in grain intercept, pore intercept and pore separation was associated with the preferential removal of the finer pore sections in the distribution although many fine pore sections remained after 12 h. Interestingly, after 12 h the density of the samples made with powder C was lower than for samples made from powder W and powder F. However, the average grain size, average pore size and average pore separation were like those samples made from powder F. The microstructure of powder C after 12 h is shown in Figure 6 (c). Here, there were a mixture of small pore sections and larger irregular pore sections. There were none

of the large dense areas observed in the materials made from powder W or the aligned pores observed for powder F. It should be noted that all the final microstructures shown in Figure 6 involves a large quantity of highly elongated and randomly coordinated pores. Exner et al. [33] once pointed out that typical Oswald ripening of pores only occurs at very late stage of sintering, and the resulting coarsened pores are highly spherical. Hence it is not likely that the remnant porosity in any of the three sintered powders resulted from Oswald ripening.

In summary, materials from all three powders densified more quickly at short times and appeared to coarsen throughout the 12 h of sintering at 1270 °C. The coarsening of the microstructure occurred by the elimination of small pore section as a result of the microstructural heterogeneity [34] and not by the growth of individual pores. The elimination of pore sections allowed the grains to grow. The wider particle size distribution in powder W seemed to “coarsen” faster and to a greater extent. The wider particle size distribution resulted in more elimination of small pore section and the larger more irregular pore sections remain.

3.2. Supersolidus liquid phase sintering

When the temperature increased to 1285 °C, supersolidus sintering occurred. Figure 7 shows the linear shrinkage for samples sintered at this temperature. Similar to Figure 2, a significant gap between *z*-shrinkage and *x/y*-shrinkage can be seen, especially for powder F.

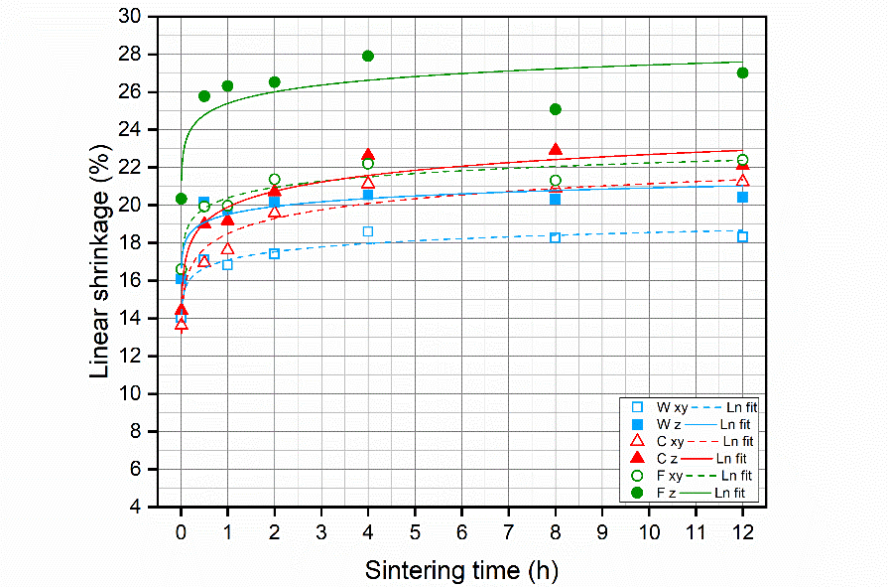

Figure 7. Linear shrinkage of samples sintered at 1285 °C for powder W, F and C, measured in *x/y*- and *z*-direction. Curves show lognormal fitting of the shrinkage.

Figure 8 shows good agreement between the bulk density and the solid area fraction measured on the micrographs. Therefore, the micrographs were considered representative. The materials made from all three powders reached densities greater than 90% within the first 2 h. The density of powder W in Figure 8 is above 95% after 1 h and

the density measurements also showed that the pores are closed after 30 min of sintering. After 12 h the microscopy analysis showed a final density above 99%.

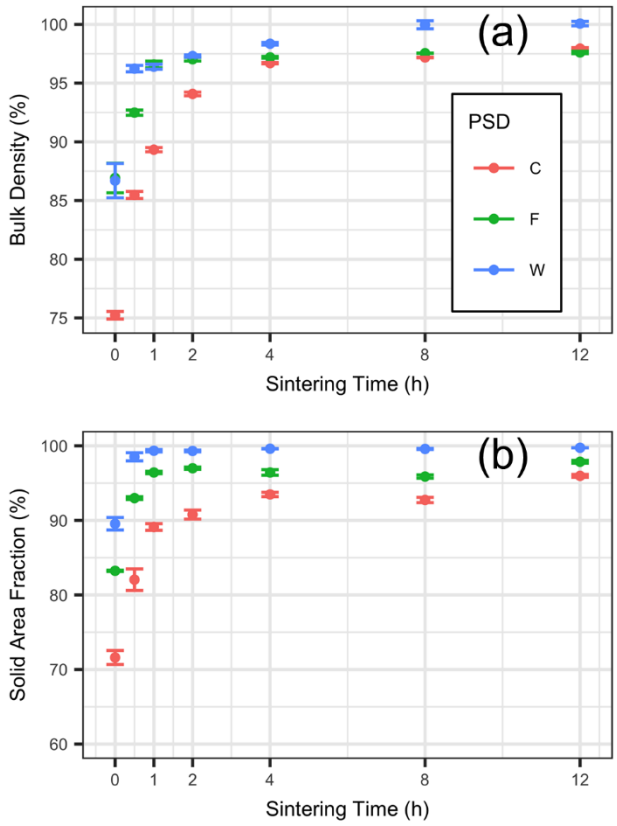

Figure 8. The effect of sintering time on (a) the relative bulk density measured by the Archimedes method and (b) solid area fraction measured on optical micrographs of polished sections for powder W, powder F and powder C sintered at 1285 °C.

Figure 9 (a) shows that the grain intercept for powder W increased from 80 μm at 0 h to over 200 μm after 12 h while the pore intercept decreased from 120 μm at 0 h to less than 10 μm for the few remaining pores. This resulted in the pore separation increasing from 300 μm to about 1.8 mm. Interestingly, the pore size reduction and pore elimination for powder W occurred concurrently with a large increase in grain intercept and pore separation. Therefore, the diffusion distance was increasing dramatically during final stage supersolidus sintering. The densification rate was enhanced due to the presence of the liquid phase and the increase in scale due to the coarsening of the microstructure did not preclude the attainment of very high density at longer sintering times. This is consistent with the 1.8 mm pore separation for powder W after 12 h which is several times larger than that for powder F and powder C sintered under the same conditions.

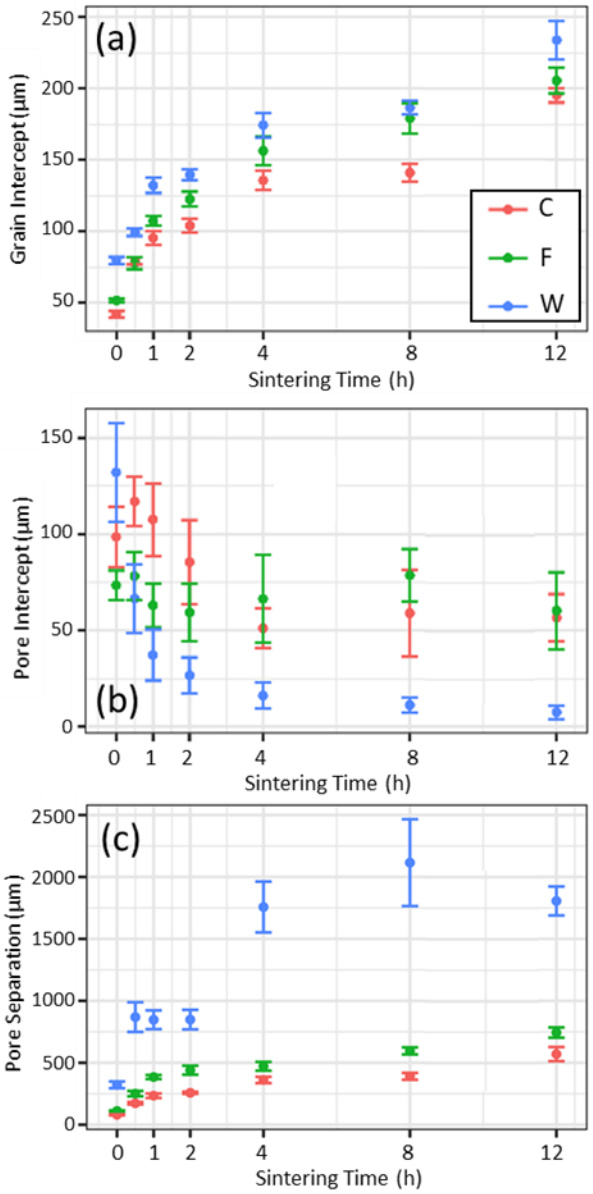

Figure 9. The effect of sintering time at 1285 °C on (a) grain intercept, (b) pore intercept and (c) pore separation for powder W, powder F and powder C.

Examination of the pore size distribution for powder W, counted by number frequency in Figure 10 (a), is relatively broad with a distinct peak at large pore sizes after 0 h. Importantly the largest pore sections in the distribution, above 1,000 μm^2 were preferentially removed within the first 0.5 h. This did not happen for subsolidus sintering and is thought to be caused by viscous rearrangement of particles under the surface tension of the wetting liquid [35]. Rearrangement of the particles reduced the number of the large packing defects in the printed material. In addition, the very small pore sections, below 30 μm^2, were also eliminated in the first 0.5 h, probably due to an enhanced rate of contact flattening in liquid phase sintering. This rearrangement behavior correlates well with the model prediction developed by Huppmann [36] and Fortes et al [37]. The fact

that the time of rearrangement is close to the largest estimate of the Fortes' model may be due to the very loose packing and planar defects of the powders, minimizing the number of possible liquid bridges formed. At longer times, this narrowed pore size distribution with a peak at 100 μm^2, is more suitable for densification by contact flattening and pore filling. In addition, Figure 10 (d) shows that when the increase in density is taken into consideration, the frequencies in all intervals were decreased during sintering. Importantly, the large pore size intervals were preferentially eliminated. This is very different from the evolution in the pore size distribution at 1270 °C and may be key to reaching high sintered densities, above 99%. The final microstructure for powder W at 1285 °C in Figure 11 (a, d) shows a relatively small number of isolated pores that were much smaller than the grains. A second phase associated with the presence of the supersolidus liquid was present at the grain boundaries.

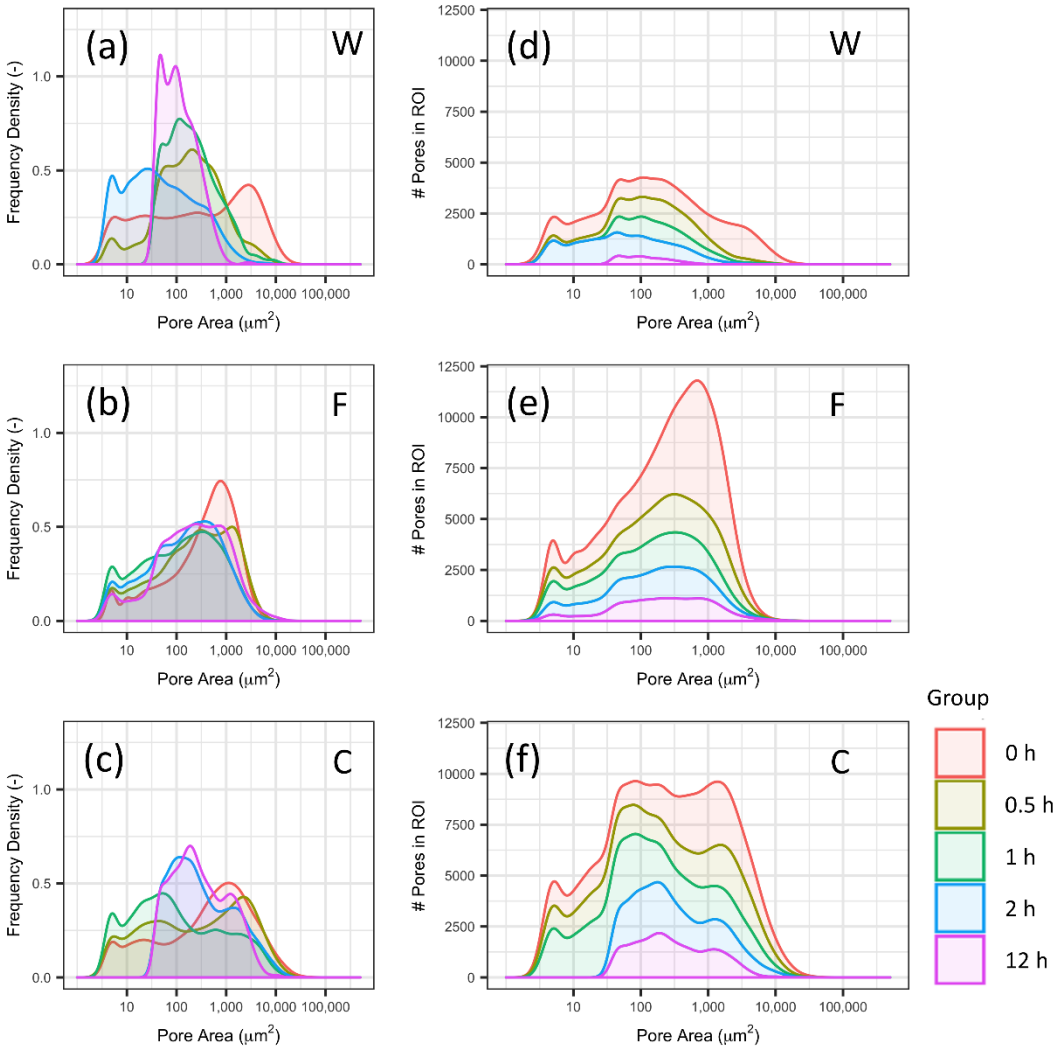

Figure 10. The pore size distributions for (a,d) powder W, (b,e) powder F, and (c,f) powder C sintered for different times ranging between 0-12 h at 1285 °C. (a-c are based on the relative number frequency whereas (d-f) are based on the absolute number count in the region of interest.

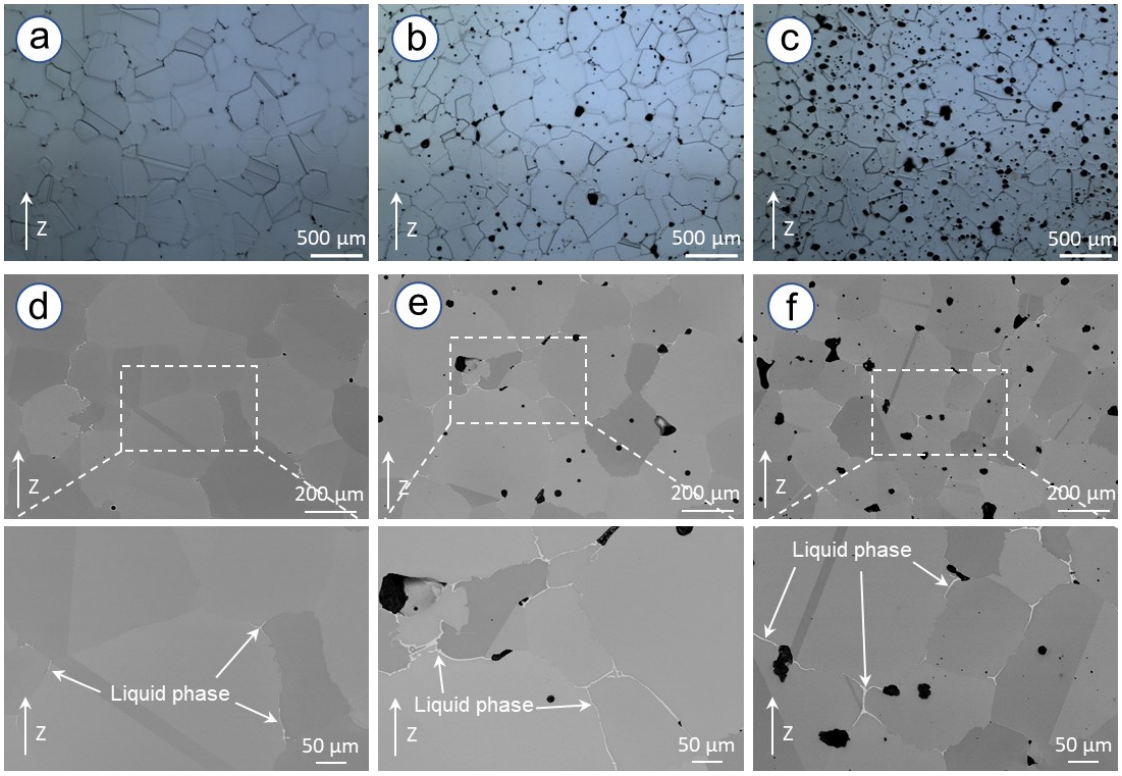

Figure 11. Micrographs of the 625 samples sintered for 12 h at 1285 °C (a, d) powder W, (16-63 µm), (b, e) powder F (16-25 µm) and (c, f) powder C, (53-63 µm). (a-c) Optical and (d-f) SEM micrographs. Liquid phase formation at the grain boundaries is shown by the white arrows. The SAF values are 99.7%, 97.9% and 96.0%, respectively.

Figure 8 (b) shows that at 1285 °C, Powder F showed an increase in density in the first 2 h, and the pores became closed after 1 h. Unlike powder W, the solid area fraction was still less than 98% after 12 h. Figure 9 (a) shows that the evolution in the grain intercept at 1285 °C was somewhat similar to powder W but the evolution in the pore size and the pore separation was very different. The pore intercept, for powder F, remains at approximately 60 µm even after 12 h and the pore separation remained below 600 µm. The pore size distribution for powder F is shown in Figure 10 (b). At 0 h, there was again a wide pore size distribution but the peak at approximately 1,000 μm^2 was much larger than for powder W. As the sintering time increases, the frequencies of the larger pores did decrease, probably by the viscous rearrangement of the particles as for powder W. Concurrent with the reduction in the frequencies of larger pores, the frequencies in the smaller pore size intervals increased. This could be due to the breakup of the large packing defects into smaller pore sections by the viscous rearrangement of particles. This would increase the number of small pore sections faster than they could be eliminated by pore filling, thereby causing the frequency to increase. This explanation is consistent with the viscous rearrangement in supersolidus sintering being faster than contact flattening and pore filling by diffusion. Unlike powder W, relatively large pore

sections did survive to longer sintering times resulting in a population of remnant pores at 12 h. This limited grain growth and the measured pore separation. The final microstructure in Figure 11 (b, e) shows the finer grains and a relatively large number of small pore sections. Such final microstructure was in good agreement with Kang et al. [38], where the pore size distribution affects densification efficiency by hindering grain growth. A grain boundary second phase was also present.

Like powder F, powder C did not reach solid area fractions above 98% after 12 h. Figure 8 shows that the density increased over a period of 4 h. The microstructure for powder C evolved like powder F. The pore size distribution is shown in Figure 10 (c, e). At shorter times, the pore size distribution was again broad with the highest peak at approximately 1,000 μm^2. The intervals of the largest sizes in the population were above 10,000 μm^2, larger than those for powder W and powder F. Like with powder W, the pore size distribution evolved by reducing the frequencies in the largest pore size intervals and the smallest pore size intervals. Again, the larger pore sections are thought to be removed by viscous rearrangement of the grains under the surface tension of the liquid and small pore sections were eliminated by contact flattening. However, the pore size distribution was bimodal after 12 h with peaks at approximately 30 μm^2 and at 1000 μm^2. In consequence, a remnant pore population was present after 12 h made up of a mixture of small and large pore sections as shown in Figure 11 (c, f). This limited the grain growth and the pore separation as for powder F. As for powder W and powder F, a second phase was observed at grain boundaries. The formation of the second phase is associated with chemical segregation, since the chemical composition in the liquid phase was quite different from the solid phases, and such difference in composition was maintained after the samples returned to room temperature, along with the solidified liquid phases. Figure 12 shows the SEM images and EDS maps for samples printed with powder W and sintered at 1270 °C for 12 h, and 1285 °C for 0 h and 12 h. It is apparent that samples sintered at 1270 °C, show little second phase or chemical segregation, as shown in Figure 12 (a). Figure 12 (b) shows evidence of Si accumulation inside the pores, which may be from the OP-S colloidal silica during final polishing steps. On the other hand, Figure 12 (c) showed a substantial amount of second phase forms in samples that were sintered just above supersolidus temperature for very short periods of time. Figure 12 (d) indicates the segregation for fast-diffusing elements such as Nb and Mo to the liquid phase. Again, this is another proof for liquid formation under 1285 °C sintering and suggests that heavy elemental segregations may have occurred during SLPS.

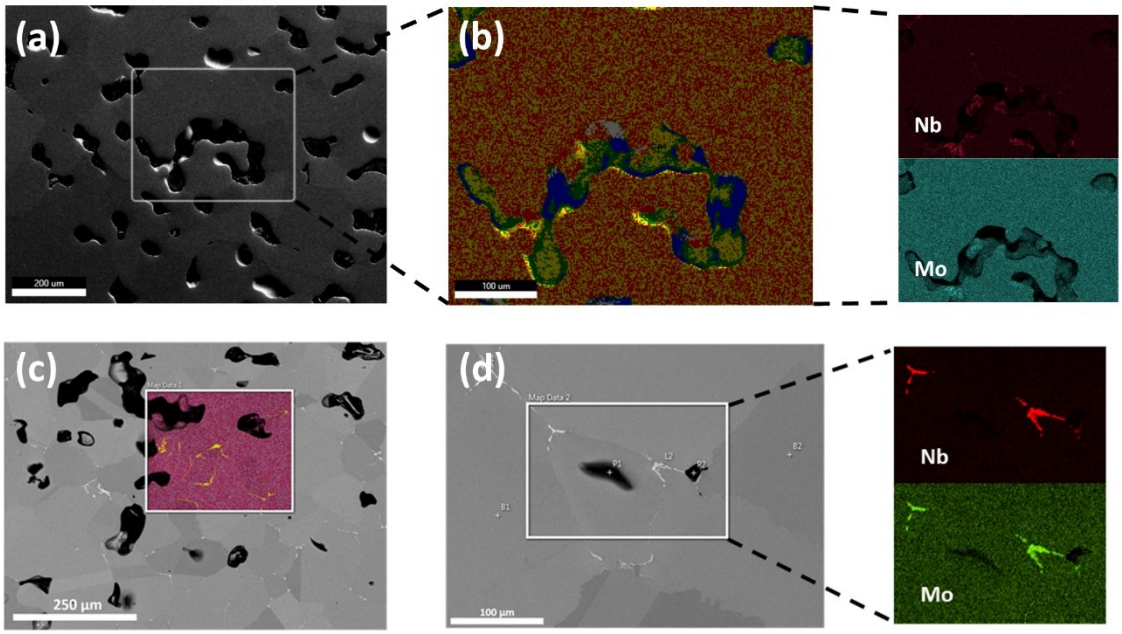

Figure 12. Scanning electron micrographs and elemental maps of selected samples sintered at 1270 °C and 1285 °C for powder W. (a) SEM micrograph for sample sintered at 1270 °C for 12 h, (b) EDS maps of a selected area showing overall elemental concentrations and segregations for Nb and Mo. (c) SEM micrograph and overlayed EDS map for sample sintered at 1285 °C for 0 h, and (d) SEM micrograph and EDS maps showing distribution of Nb and Mo for sample sintered at 1285 °C for 12 h.

4. Discussion

When atomized metal powders are binder jetted, the green densities are low, ranging between ~40-60%, depend on powder characteristics such as particle shape and size distribution. In addition, particle packing defects can be produced by powder flow during dispensing and by powder-binder interaction, inter-particle forces, and surface chemistry during jetting [3,5,39–41]. Thus, controlling these variables is essential to attain high green density, and consequently, better dimensional control and low sintering temperatures. Measured green densities for the powders W, F and C were about 52%, 45% and 48%, respectively. It is thought the differences in green density could be associated with powder particle interactions during layer spreading. Moreover, powder-binder interaction during jetting also influences particle packing, and potential inter layer defect formation. As shown by Parab et al. [26], ejection of powder particles occurs during binder spraying from the print head when a high velocity binder droplet impacts the powder bed during printing. Depending on powder size and morphology, different powder-binder interactions occurred. Fine powder particles resulted in a much larger interaction depth than coarse powder, leaving a layer of particle packing defects within each printed layer. Clearly the printed microstructure is influenced by the particle size distribution. This

study is focused on the consequences of this on the microstructural evolution during isothermal sintering above and below the solidus temperature.

Figure 13 shows the schematic representations of the microstructural evolution during supersolidus and subsolidus sintering for powder W used in this study. The area enclosed with the dashed line box indicates the inter-layer spacings between two jetted layers, which is more defective comparing with the powder packing inside each jetted layer. In microstructure path *(a)*, when the system reaches isothermal sintering temperature under the solidus, densification depends solely on neck growth by solid state sintering mechanisms *(a_1)*. It can be seen that small pores will be eliminated but large pores will remain in all the microstructures despite substantial grain growth. This microstructure evolution corresponds to the final microstructure shown in a_2. When samples are sintered at 1285 °C, the liquid phase begins to form at the neck areas when reached isothermal temperature, which is illustrated in *(b_1)*. This facilitates the viscous particle rearrangement, mostly by the displacement of small particles. This results in the collapse of the larger packing defects and a more homogeneous microstructure; hence the large pore sections are eliminated quickly. On further sintering at 1285 °C (b_2) the more homogeneous microstructure produced by particle rearrangement can continue to densify by conventional diffusional mechanisms assisted by the presence of the liquid phase, resulting in a pore-free microstructure and high final density.

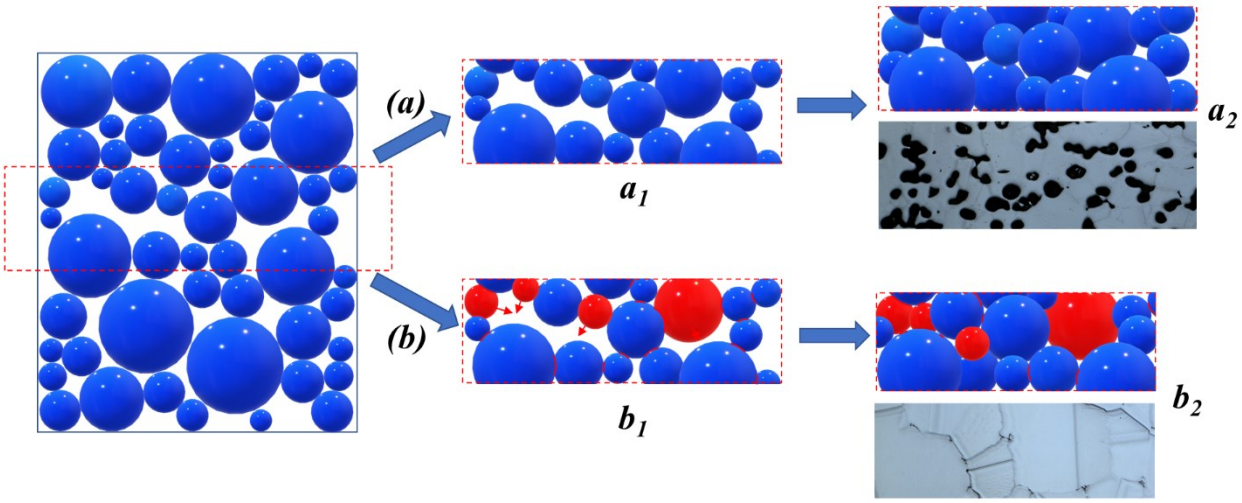

Figure 13. Schematic illustrating the paths of microstructure evolution of powder W under subsolidus sintering (a) and supersolidus sintering (b). Arrows indicate rearrangement of powder particles during supersolidus sintering and red spheres show the rearranged particles.

5. Conclusions

Binder jet printing produces heterogeneous green microstructures and the extent of the heterogeneity is affected by PSD. In consequence, the effect of PSD on the subsolidus and supersolidus isothermal sintering of binder jet printed alloy 625 can be more clearly understood from quantitative studies of microstructural evolution. The following conclusions have been made:

1. Subsolidus sintering of the heterogeneous green microstructures produced by binder jet printing resulted in solid state densification at 1270 °C with enhanced coarsening of the microstructure by the elimination of fine pores accompanied by grain growth. As a result, the diffusion distance for densification rose quickly and solid-state sintering did not achieve final stage for any of the powders used, even after 12 hours.

2. Supersolidus sintering for samples made with powder W (16-63 μm) at 1285 °C gave rapid removal of the larger pore sections with areas above 1000 μm^2 and resulted in a narrower pore size distribution in the microstructure. This is thought to be due to particle rearrangement under the surface tension of the liquid phase. Consequent liquid phase sintering by diffusional mechanisms was then able to achieve sintered densities above 99% at longer sintering times.

3. Supersolidus sintering of powder F (16-25 μm) and powder C (53-63 μm) at 1285 °C did not remove all the pore sections larger than 1000 μm^2 early in sintering. Consequent liquid phase sintering resulted in preferential elimination of fine pores and lower sintered densities than powder W at longer sintering times. This was explained in terms of the defects in the as-printed microstructure for powder F and the lower driving force for sintering of powder C.

4. Supersolidus sintering resulted in a grain boundary phase retained at room temperature.

Acknowledgement

This project was funded in part by a grant from the Pennsylvania Department of Community & Economic Development through the Manufacturing PA Initiative as well as the Air Force Research Laboratory under agreement number FA8650-12-2-7230 and by the Commonwealth of Pennsylvania, acting through the Pennsylvania Department of Community and Economic Development, under contract number C000053981. This work was performed, in part, at the Nanoscale Fabrication and Characterization Facility, a laboratory of the Gertrude E. and John M. Petersen Institute of NanoScience and Engineering, and the Materials Micro-Characterization Laboratory both housed at the University of Pittsburgh. PRDV appreciates partial funding through the NSF REU supplemental funding of award 1727676.

References

[1] A. Mostafaei, A.M. Elliott, J.E. Barnes, F. Li, W. Tan, C.L. Cramer, P. Nandwana, M. Chmielus, Binder jet 3D printing—Process parameters, materials, properties, modeling, and challenges, Progress in Materials Science. 119 (2021). https://doi.org/10.1016/j.pmatsci.2020.100707.

[2] A. Mostafaei, E.L. Stevens, J.J. Ference, D.E. Schmidt, M. Chmielus, Binder jetting of a complex-shaped metal partial denture framework, Additive Manufacturing. 21 (2018) 63–68. https://doi.org/10.1016/j.addma.2018.02.014.

[3] P. Nandwana, A.M. Elliott, D. Siddel, A. Merriman, W.H. Peter, S.S. Babu, Powder bed binder jet 3D printing of Inconel 718: Densification, microstructural evolution and challenges, Current Opinion in Solid State and Materials Science. 21 (2017) 207–218. https://doi.org/10.1016/j.cossms.2016.12.002.

[4] A. Mostafaei, J. Toman, E.L. Stevens, E.T. Hughes, Y.L. Krimer, M. Chmielus, Microstructural evolution and mechanical properties of differently heat-treated binder jet printed samples from gas- and water-atomized alloy 625 powders, Acta Materialia. 124 (2017) 280–289. https://doi.org/10.1016/j.actamat.2016.11.021.

[5] A. Mostafaei, Y. Behnamian, Y.L. Krimer, E.L. Stevens, J.L. Luo, M. Chmielus, Effect of solutionizing and aging on the microstructure and mechanical properties of powder bed binder jet printed nickel-based superalloy 625, Materials and Design. 111 (2016) 482–491. https://doi.org/10.1016/j.matdes.2016.08.083.

[6] E. Wheat, Process Mapping and Optimization of Titanium Parts Made by Binder Jetting Additive Manufacturing, 2018.

[7] E. Sheydaeian, Z. Fishman, M. Vlasea, E. Toyserkani, On the effect of throughout layer thickness variation on properties of additively manufactured cellular titanium structures, Additive Manufacturing. 18 (2017) 40–47. https://doi.org/10.1016/j.addma.2017.08.017.

[8] J.J.S. Dilip, H. Miyanaji, A. Lassell, T.L. Starr, B. Stucker, A novel method to fabricate TiAl intermetallic alloy 3D parts using additive manufacturing, Defence Technology. 13 (2017) 72–76. https://doi.org/10.1016/j.dt.2016.08.001.

[9] D. Hong, D.T. Chou, O.I. Velikokhatnyi, A. Roy, B. Lee, I. Swink, I. Issaev, H.A. Kuhn, P.N. Kumta, Binder-jetting 3D printing and alloy development of new biodegradable Fe-Mn-Ca/Mg alloys, Acta Biomaterialia. 45 (2016) 375–386. https://doi.org/10.1016/j.actbio.2016.08.032.

[10] A. Levy, A. Miriyev, A. Elliott, S.S. Babu, N. Frage, Additive manufacturing of complex-shaped graded TiC/steel composites, Materials & Design. 118 (2017) 198–203. https://doi.org/10.1016/j.matdes.2017.01.024.

[11] D.S.D. Uduwage, Binder Jet Additive Manufacturing of Stainless Steel-Hydroxyapatite Bio-composite, 2015. https://doi.org/10.1.1.922.9174.

[12] M. Doyle, K. Agarwal, W. Sealy, K. Schull, Effect of Layer Thickness and Orientation on Mechanical Behavior of Binder Jet Stainless Steel 420 + Bronze Parts, in: Procedia Manufacturing, Elsevier B.V., 2015: pp. 251–262. https://doi.org/10.1016/j.promfg.2015.09.016.

[13] Y. Tang, Y. Zhou, T. Hoff, M. Garon, Y.F. Zhao, Elastic modulus of 316 stainless steel lattice structure fabricated via binder jetting process, Materials Science and Technology (United Kingdom). 32 (2016) 648–656. https://doi.org/10.1179/1743284715Y.0000000084.

[14] T. Do, P. Kwon, C.S. Shin, Process development toward full-density stainless steel parts with binder jetting printing, International Journal of Machine Tools and Manufacture. 121 (2017) 50–60. https://doi.org/10.1016/j.ijmachtools.2017.04.006.

[15] A. Mostafaei, P.R. de Vecchis, M.J. Buckenmeyer, S.R. Wasule, B.N. Brown, M. Chmielus, Microstructural evolution and resulting properties of differently sintered and heat-treated binder jet 3D printed Stellite 6, Materials Science and Engineering: C. 102 (2019) 276–288.

[16] J.W. Sears, C. Allen, A. Holliday, Binder-Jet 3D Direct Metal Printing of Cobalt Chrome Moly Alloy, AMPM 2019 Conference, Phoenix, Arizona. (2019).

[17] A. Mostafaei, P. Rodriguez De Vecchis, E.L. Stevens, M. Chmielus, Sintering regimes and resulting microstructure and properties of binder jet 3D printed Ni-Mn-Ga magnetic shape memory alloys, Acta Materialia. 154 (2018) 355–364. https://doi.org/10.1016/j.actamat.2018.05.047.

[18] A. Mostafaei, K.A. Kimes, E.L. Stevens, J. Toman, Y.L. Krimer, K. Ullakko, M. Chmielus, Microstructural evolution and magnetic properties of binder jet additive manufactured Ni-Mn-Ga magnetic shape memory alloy foam, Acta Materialia. 131 (2017) 482–490. https://doi.org/10.1016/j.actamat.2017.04.010.

[19] M.P. Caputo, A.E. Berkowitz, A. Armstrong, P. Müllner, C.V. Solomon, 4D printing of net shape parts made from Ni-Mn-Ga magnetic shape-memory alloys, Additive Manufacturing. 21 (2018) 579–588. https://doi.org/10.1016/j.addma.2018.03.028.

[20] M.P. Caputo, C. v. Solomon, A facile method for producing porous parts with complex geometries from ferromagnetic Ni-Mn-Ga shape memory alloys, Materials Letters. 200 (2017) 87–89. https://doi.org/10.1016/j.matlet.2017.04.112.

[21] A. Kumar, Y. Bai, A. Eklund, C.B. Williams, Effects of Hot Isostatic Pressing on Copper Parts Fabricated via Binder Jetting, Procedia Manufacturing. 10 (2017) 935–944.

[22] A. Yegyan Kumar, J. Wang, Y. Bai, S.T. Huxtable, C.B. Williams, Impacts of process-induced porosity on material properties of copper made by binder jetting additive manufacturing, Materials & Design. 182 (2019) 108001. https://doi.org/10.1016/j.matdes.2019.108001.

[23] H. Miyanaji, D. Ma, M.A. Atwater, K.A. Darling, V.H. Hammond, C.B. Williams, Binder Jetting Additive Manufacturing of Copper Foam Structures, Additive Manufacturing. 32 (2020) 100960. https://doi.org/https://doi.org/10.1016/j.addma.2019.100960.

[24] Y. Zhu, Z. Wu, W.D. Hartley, J.M. Sietins, C.B. Williams, H.Z. Yu, Unraveling Pore Evolution in Post-Processing of Binder Jetting Materials: X-Ray Computed Tomography, Computer Vision, and Machine Learning, Additive Manufacturing. (2020). https://doi.org/10.1016/j.addma.2020.101183.

[25] E. Sachs, M. Cima, J. Cornie, D. Brancazio, J. Bredt, A. Curodeau, T. Fan, S. Khanuja, A. Lauder, J. Lee, S. Michaels, Three-Dimensional Printing: The Physics and Implications of Additive Manufacturing, CIRP Annals - Manufacturing Technology. 42 (1993) 257–260. https://doi.org/10.1016/S0007-8506(07)62438-X.

[26] N.D. Parab, J.E. Barnes, C. Zhao, R.W. Cunningham, A.D. Rollett, T. Sun, Real time observation of binder jetting printing process using high-speed X-ray imaging, Scientific Reports. (2019) 28–30.

[27] A. Mostafaei, P. Rodriguez De Vecchis, I. Nettleship, M. Chmielus, Effect of powder size distribution on densification and microstructural evolution of binder-jet 3D-printed alloy 625, Materials and Design. 162 (2019) 375–383. https://doi.org/10.1016/j.matdes.2018.11.051.

[28] D. Huber, L. Vogel, A. Fischer, The Effects of Sintering Temperature and Hold Time on Densification, Mechanical Properties and Microstructural Characteristics of Binder Jet 3D Printed 17-4 PH Stainless Steel, Additive Manufacturing. (2020) 102114. https://doi.org/10.1016/j.addma.2021.102114.

[29] A. Mostafaei, E.L. Stevens, E.T. Hughes, S.D. Biery, C. Hilla, M. Chmielus, Powder bed binder jet printed alloy 625: Densification, microstructure and mechanical properties, Materials and Design. 108 (2016) 126–135. https://doi.org/10.1016/j.matdes.2016.06.067.

[30] G.E. Pellissier, S.M. Purdy, Stereology and Quantitative Metallography, in: ASTM Spec. Tech. Publ., 1972: p. 138.

[31] I. Nettleship, T. Chen, K. Ewsuk, Characterization of Heterogeneous Microstructure Evolution in ZrO2-3 mol%Y2O 3 during Isothermal Sintering, Journal of the American Ceramic Society. 90 (2007) 3793–3799. https://doi.org/10.1111/j.1551-2916.2007.02052.x.

[32] T. Chen, I. Nettleship, R.J. Mcafee, T.R. Hinklin, K.G. Ewsuk, An Experimental Measurement of Effective Diffusion Distance for the Sintering of Ceramics, Journal American Ceramic Society. 92 (2009) 1481–1486. https://doi.org/10.1111/j.1551-2916.2009.02954.x.

[33] H.E. Exner, C. Müller, Particle rearrangement and pore space coarsening during solid-state sintering, Journal of the American Ceramic Society. 92 (2009) 1384–1390. https://doi.org/10.1111/j.1551-2916.2009.02978.x.

[34] J. Zhao, M.P. Harmer, Effect of Pore Distribution on Microstructure Development: II, First- and Second-Generation Pores, Journal of the American Ceramic Society. 71 (1988) 530–539. https://doi.org/10.1111/j.1151-2916.1988.tb05916.x.

[35] J. Liu, R.M. German, Rearrangement densification in liquid-phase sintering, Metallurgical and Materials Transactions A: Physical Metallurgy and Materials Science. 32 (2001) 3125–3131. https://doi.org/10.1007/s11661-001-0187-6.

[36] W.J. Huppmann, H. Riegger, Modelling of Rearrangement Processes in Liquid Phase Sintering, Acta Metallurgica. 23 (1975) 965–971.

[37] M.A. Fortes, The Kinetics of Powder Densification Due to Capillary Forces, Powder Metallurgy International. 14 (1982) 96–100.

[38] S.-J.L. Kang, Sintering: Densification, Grain Growth and Microstructure, Elsevier, 2004.

[39] R.M. German, Particle Packing Characteristics, Metal Powder Industries Federation, Princeton N.J, 1989.

[40] A. Mostafaei, E.T. Hughes, C. Hilla, E.L. Stevens, M. Chmielus, Data on the densification during sintering of binder jet printed samples made from water- and gas-atomized alloy 625 powders, Data in Brief. 10 (2017) 116–121. https://doi.org/10.1016/j.dib.2016.11.078.

[41] A.M. Elliott, P. Nandwana, D. Siddel, B.G. Compton, A Method for Measuring Powder Bed Density in Binder Jet Additive Manufacturing Process and the Powder Feedstock Characteristics Influencing the Powder Bed Density, Oak Ridge, TN (United States), 2017. http://energy.gov/downloads/doe-public-access-plan.